Room-temperature antiferromagnetic order in monolayer Fe$_2$C

N. Fathizadeh [,1] M. Modarresi [,1,*] M. R. Roknabadi [,1] J. Pawłowski [,2] and A. Mogulkoc [3]

[1]*Department of Physics, Faculty of Science, Ferdowsi University of Mashhad, 91775-1436, Mashhad, Iran*
[2]*Department of Theoretical Physics, Wrocław University of Science and Technology,*
Wybrzeże Wyspiańskiego 27, 50-370 Wrocław, Poland
[3]*Department of Physics, Faculty of Sciences, Ankara University, 06100 Tandogan, Ankara, Turkey*

We have studied the room-temperature long-range antiferromagnetic order in the Fe$_2$C monolayer using the combination of first-principles calculations and the Green's function analysis within the anisotropic Heisenberg model. The Fe$_2$C monolayer is a semimetal with the out-of-plane antiferromagnetic order between two Fe planes. The Green's function approach within the random phase approximation is formulated to calculate the temperature-dependent antiferromagnetic magnon energy and the spin correlation function in a two-dimensional antiferromagnetic monolayer. The correlation function is used to evaluate the sublattice magnetization and study the magnetic phase transition in monolayer Fe$_2$C. Moreover, the spin Hamiltonian and the Green's function formalism are developed to investigate the antiferromagnetic Fe$_2$C monolayer in the presence of an external magnetic field applied along the easy axis. The H-T phase diagram shows that the antiferromagnetic to spin-flop and the spin-flop to paramagnetic phase transitions occur in low temperatures. Finally, we estimate the Néel temperature and the critical values of the magnetic field strength for these two phase transitions.

I. INTRODUCTION

Since the discovery of graphene, two-dimensional (2D) materials have received great attention because of their peculiar electronic and magnetic properties and vast technological applications (e.g., spintronics, storage energy devices, and quantum computing) [1]. The 2D monolayers can be isolated from the bulk layered materials. The layers of these materials are bonded by either weak van der Waals (vdW) or covalent interactions, where strong forces hold the atoms together within the layers. For some decades, the existence of a long-range magnetic order in 2D materials remained elusive. In the meantime, many techniques have been drawn to induce magnetic order into 2D materials by changing the crystal structure, in particular, by using localized defects, doping, adsorption of magnetic atoms, or proximity effect. The restriction of these methods in the application of 2D materials, including difficulty to achieve a homogeneous distribution of defects/dopants/adatoms, low critical temperatures, and limitations of atoms adsorption in monolayers, has motivated a discovery of intrinsically two-dimensional magnetic materials [2–8].

The Mermin-Wagner-Hohenberg theorem states that thermal fluctuations exclude long-range magnetic order in one- and two-dimensional isotropic Heisenberg magnets with short-range exchange interactions [9,10]. The magnetic anisotropy is crucial in 2D materials to prevent the thermal fluctuations and stabilize 2D long-range intrinsic magnetism [11–17]. The dependence of magnetic phases on the number of layers has been found in vdW CrI$_3$: ferromagnetic (FM) order in the monolayer, antiferromagnetic (AFM) order in the bilayer, and, again, FM order in the trilayer [14]. The long-range AFM order with a low transition temperature has been first observed in bilayer Cr$_2$Ge$_2$Te$_6$. It has been found that the transition temperature can be controlled by using a low magnetic field and the observed phenomena are explained by using the renormalized spin-wave theory [13]. The Fe$_2$N monolayer with a square lattice can be synthesized on a Cu substrate. It is found that monolayer Fe$_2$N exhibits FM order with in-plane magnetic anisotropy [18]. The long-range 2D FM order is observed for VSe$_2$ and MNSe$_2$ above room temperature [19,20]. To date, several 2D magnetic materials with various chemical compositions have been synthesized with different methods [18–26]. Predicting and designing new 2D monolayers with intrinsic magnetic order is an interesting research field in theoretical physics nowadays. These research results show that 2D materials have possessed the long-range magnetic order down to the monolayer limit because of the presence of magnetic anisotropy, which arises from the spin-orbit interaction [27–40].

AFM materials are more appropriate than FM materials for spintronic applications because of the large magnetoresistance transport, higher switching frequencies, and high speed operation. AFM materials, unlike FMs, do not generate redundant magnetic fields that can affect the general operation and restrict the smallest possible size of a device. Moreover, AFM materials are insensible to an undesired magnetic field because of zero net magnetization [41–46]. Nevertheless, the AFM 2D materials have been remarkably less researched, in contrast to the FM monolayer materials. Some limited studies indicate that FePS$_3$ exhibits an AFM behavior from bulk to

*m.modarresi@um.ac.ir

the monolayer limit, with the Néel temperature independent of the layer thickness [47,48]. Raman spectroscopy shows that the magnetic order of $NiPS_3$ and $MnPS_3$ is of the AFM type in bulk and remains the same down to two layers. For $MnPS_3$, tunneling magnetoresistance measurements indicate the AFM order at the monolayer limit [49,50]. The AFM order has also been detected in tetragonal FeTe thin flakes where the Néel temperature is reduced from 70 to 45 K [26].

Besides the thermal fluctuations, it is widely known that an applied magnetic field H also can disrupt the AFM order. At sufficiently low temperatures, when the H field parallel to the easy-axis direction reaches a critical value, spins suddenly realign perpendicular to the H direction, known as a spin-flop phase. The AFM to spin-flop phase transition occurs when the anisotropy energy is much weaker than the exchange interaction. In this situation, the antiferromagnetic coupling between spins is maintained while spins are rotated. Indeed, the magnetic field energy overcomes the magnetic anisotropy energy, but not the exchange interaction. The spin-flop phase has great potential to be employed in AFM spintronic applications [51,52].

Here, we study the persistence of the long-range AFM order in monolayer Fe_2C by using the combination of first-principles calculations and the Green's function method. The Fe_2C monolayer is a member of the *MX*ene family of 2D transition metal carbides, nitrides, and carbonitrides with the formula of $M_{n+1}X_n$. The noncollinear *ab initio* results are mapped into an anisotropic Heisenberg model to derive effective parameters. The temperature dependence of sublattice magnetization and the transition temperature T_N are investigated within the random phase approximation (RPA) [53–55]. The present formalism is general and can be used to study other 2D monolayers with AFM order. The paper is organized as follows. Section II A provides the details of density functional theory (DFT) calculations for the Fe_2C monolayer, while Sec. II B introduces the Green's function formalism within RPA to describe the thermodynamics of AFM monolayers in the presence of an external magnetic field. In Sec. III, we apply the Green's function method to monolayer Fe_2C and investigate the magnetic properties of monolayer Fe_2C in the absence/presence of an external magnetic field. Finally, a brief summary and conclusion are provided in Sec. IV.

II. METHOD AND MODEL

We start by introducing the details of the DFT + U calculations, then we provide the Green's function formalism that is used.

A. Density functional theory calculations

The DFT + U calculations are performed by applying the Hubbard U correction on Fe-3d electronic states as implemented in the QUANTUM ESPRESSO package [56,57]. The ultrasoft atomic pseudopotentials and the revised Perdew-Burke-Ernzerhof functional for solids (PBEsol) are used to treat the electron-ion interactions and the exchange correlation interactions, respectively. The cutoff energy for expansion of wave functions is set to 140 Ry and we consider 1400 Ry for the calculation of the electronic density. The electronic self-
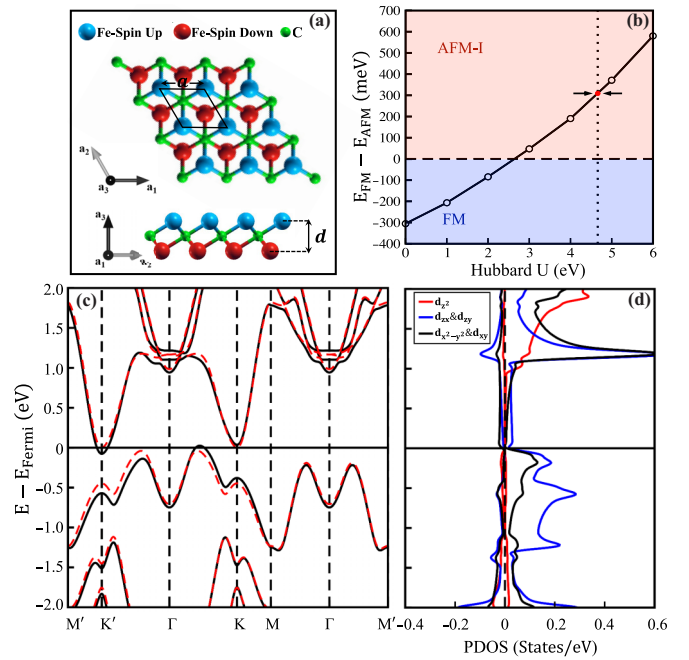

FIG. 1. (a) The top and side view of the T-phase atomic structure of monolayer Fe_2C. The blue/red and green spheres display Fe with spin up/down and C atoms, respectively. (b) The variation of the energy difference between FM and AFM-1 states with Hubbard U parameter. (c) The electronic band structure of monolayer Fe_2C calculated using DFT + U with (black solid lines) and without (red dashed lines) the SOC effect. (d) The density of states for monolayer Fe_2C projected on atomic orbitals of a spin-up Fe atom in the AFM-1 ground state. The horizontal black line in (c) and (d) indicates the Fermi level energy which is set to zero.

consistent convergence threshold is set to 10^{-8} Ry. The first Brillouin zone is sampled by a $19 \times 19 \times 1$ Monkhorst-Pack k-point grid [58]. The electronic density of states is computed within a dense k-point mesh of $38 \times 38 \times 1$. We consider a T-phase hexagonal atomic structure of monolayer Fe_2C, where the C atom layer is sandwiched between the two Fe layers. The C atom is at the center of a hexagonal formed by six neighboring Fe atoms, as shown in Fig. 1(a). In the FM state, all Fe spins are oriented in the same direction. In monolayer Fe_2C with AFM order, the Fe atoms have the opposite spin direction, resulting in the net magnetization being zero. To find the magnetic ground state, we consider a supercell containing 2×2 unit cells with four spin arrangements, i.e., FM, AFM-1, AFM-2, and AFM-3 (see Figs. S1(a)–S1(d) in the Supplemental Material [59]). A vacuum of 15 Å is implanted between the two adjacent Fe_2C monolayers to avoid artificial interaction between periodic image layers. The lattice constant and the atomic positions are optimized by using the Broyden-Fletcher-Goldfarb-Shanno algorithm [60] until the force on each atom is less than 10^{-5} Ry/Bohr. The Hubbard correction in the DFT + U method is related to the strongly correlated electronic structure of Fe-3d atomic orbitals, which can change the ground-state properties [61–64]. The Hubbard U parameter is calculated self-consistently within the linear response approximation based on the density functional perturbation theory (DFPT) [65–67]. In the linear response

approximation, the Hubbard U parameter is derived from the perturbative response of occupation states to a small shift in the potential. The nonorthogonalized atomic orbitals are used as the projector functions to construct the Hubbard manifold. The DFPT calculation is carried out with a $4 \times 4 \times 1$ mesh to sample the reciprocal space.

B. The Green's function approach to the anisotropic Heisenberg spin model

The most popular model used for AFM materials is the two-sublattice model. In this model, a lattice is considered as two identical interpenetrating sublattices, labeled A and B, with opposite magnetic moments [68],

$$
\mathcal{H} = \sum_{i \in A} \sum_{j \in B} J_{i,j} \left[S_i^z S_j^z + \frac{1}{2}(S_i^+ S_j^- + S_i^- S_j^+) \right]
$$
$$
- D\left(\sum_{i \in A} S_i^z S_i^z + \sum_{j \in B} S_j^z S_j^z \right) - \mu H\left(\sum_{i \in A} S_i^z + \sum_{j \in B} S_j^z \right).
$$
(1)

In the Heisenberg spin model [Eq. (1)], the first term describes the isotropic magnetic exchange interaction, where J_{ij} is the exchange interaction coupling between the ith and jth magnetic moment, S_i is the spin operator associated with the ion at site i with component (S_i^x, S_i^y, S_i^z), and $S_i^\pm = S_i^x \pm i S_i^y$. The second term introduces the single-ion magnetic anisotropy on the A and B sublattices. The last term

is the Zeeman energy for each sublattice in an external applied magnetic field H, which is considered perpendicular to the monolayer plane. The magnetic exchange and single-ion anisotropy parameters for monolayer Fe_2C are determined using finite energy differences obtained from the DFT $+ U$ results.

To investigate the thermodynamic behavior of the magnetic monolayer, the retarded double-time temperature-dependent Green's function [69] is used,

$$
\langle\langle S_{\lambda l}^+(t); e^{a S_{\mu m}^z(t')} S_{\mu m}^-(t') \rangle\rangle
$$
$$
= -i\theta(t-t')\langle [S_{\lambda l}^+(t); e^{a S_{\mu m}^z(t')} S_{\mu m}^-(t')] \rangle,
$$
(2)

where $S_{\lambda l}$ is the time-dependent spin operator for magnetic ion at site l in sublattice λ, and a is an arbitrary parameter. The square brackets, single-angle brackets, and double-angle brackets denote commutation relations, the thermal average over the canonical ensemble, and the Green's function, respectively. The $\theta(t)$ is the step function, which takes 1 for $t > 0$ and 0 for $t < 0$.

The equation of motion for the Fourier transform of the Green's function with respect to time is [69]

$$
E\langle\langle S_{\lambda l}^+; e^{a S_{\mu m}^z} S_{\mu m}^- \rangle\rangle_E
$$
$$
= \frac{\langle [S_{\lambda l}^+, e^{a S_{\mu m}^z} S_{\mu m}^-] \rangle}{2\pi} \delta_{\lambda l, \mu m} + \langle\langle [S_{\lambda l}^+, \mathcal{H}]; e^{a S_{\mu m}^z} S_{\mu m}^- \rangle\rangle_E.
$$
(3)

Due to the anisotropic Heisenberg Hamiltonian, given by Eq. (1), and the spin commutation relationships, the equation of motion can be rewritten as

$$
(E - \mu H)\langle\langle S_{\lambda l}^+; e^{a S_{\mu m}^z} S_{\mu m}^- \rangle\rangle = \frac{\langle [S_{\lambda l}^+, e^{a S_{\mu m}^z} S_{\mu m}^-] \rangle}{2\pi} \delta_{\lambda l, \mu m} + 2\sum_{v \in n} J_{\lambda l, vn} \langle\langle (S_{\lambda l}^z S_{vn}^+ - S_{\lambda l}^+ S_{vn}^z); e^{a S_{\mu m}^z} S_{\mu m}^- \rangle\rangle
$$
$$
+ D\langle\langle (S_{\lambda l}^+ S_{\lambda l}^z + S_{\lambda l}^z S_{\lambda l}^+); e^{a S_{\mu m}^z} S_{\mu m}^- \rangle\rangle \quad (\lambda \neq v),
$$
(4)

where the E subscript for the Green's function is dropped for simplicity. The λ, μ, and v are referred to each A and B sublattice where $\lambda \neq v$. The exchange term, $\langle\langle (S_{\lambda l}^z S_{vn}^+ - S_{\lambda l}^+ S_{vn}^z); e^{a S_{\mu m}^z} S_{\mu m}^- \rangle\rangle$, and the anisotropy term, $\langle\langle (S_{\lambda l}^+ S_{\lambda l}^z + S_{\lambda l}^z S_{\lambda l}^+); e^{a S_{\mu m}^z} S_{\mu m}^- \rangle\rangle$, contain the higher-order Green's functions that satisfy an analogous equation of motion. The RPA is adopted for decoupling the exchange term in Eq. (4) into the Green's function $\langle\langle S_{\lambda l}^+; e^{a S_{\mu m}^z} S_{\mu m}^- \rangle\rangle$. In the RPA scheme, the spin correlation between $S_{\lambda l}^z$ and S_{vn}^+ (for $\lambda l \neq vn$) is disregarded and the $S_{\lambda l}^z$ operator is substituted by its average value $\langle S_{\lambda l}^z \rangle$,

$$
\langle\langle S_{\lambda l}^z S_{vn}^+; e^{a S_{\mu m}^z} S_{\mu m}^- \rangle\rangle \xrightarrow{\lambda l \neq vn} \langle S_{\lambda l}^z \rangle \langle\langle S_{vn}^+; e^{a S_{\mu m}^z} S_{\mu m}^- \rangle\rangle.
$$
(5)

For the anisotropy term, we take the decoupling scheme used by Narath [70] that is equivalent to Eq. (5),

$$
\langle\langle (S_{\lambda l}^+ S_{\lambda l}^z + S_{\lambda l}^z S_{\lambda l}^+); e^{a S_{\mu m}^z} S_{\mu m}^- \rangle\rangle \longrightarrow 2\langle S_{\lambda l}^z \rangle \langle\langle S_{\lambda l}^+; e^{a S_{\mu m}^z} S_{\mu m}^- \rangle\rangle.
$$
(6)

By using the RPA [Eq. (5)] and the Narath approximation [Eq. (6)], one can write the equation of motion for the Green's function as

$$
(E - \mu H)\langle\langle S_{\lambda l}^+; e^{a S_{\mu m}^z} S_{\mu m}^- \rangle\rangle = \frac{\langle [S_{\lambda l}^+, e^{a S_{\mu m}^z} S_{\mu m}^-] \rangle}{2\pi} \delta_{\lambda l, \mu m} + 2\sum_{n \in v} J_{\lambda l, vn} \left(\langle S_{\lambda l}^z \rangle \langle\langle S_{vn}^+; e^{a S_{\mu m}^z} S_{\mu m}^- \rangle\rangle - \langle S_{vn}^z \rangle \langle\langle S_{\lambda l}^+; e^{a S_{\mu m}^z} S_{\mu m}^- \rangle\rangle \right)
$$
$$
+ 2D\langle S_{\lambda l}^z \rangle \langle\langle S_{\lambda l}^+; e^{a S_{\mu m}^z} S_{\mu m}^- \rangle\rangle \quad (\lambda \neq v).
$$
(7)

Here, for the ground state of monolayer Fe_2C with AFM order, Eq. (7) is solved in the absence of an external magnetic field at a finite temperature. We also

investigate the effect of a perpendicular magnetic field on the thermodynamics of monolayer Fe_2C in the following sections.

III. RESULTS AND DISCUSSION

The DFT + U calculations are performed for the T-phase atomic configuration of monolayer Fe_2C as shown in Fig. 1(a). The Hubbard U parameter is evaluated from the self-consistent linear response method and converged to $U_{LR} = 4.66$ eV (see Fig. S2 in the Supplemental Material [59]). The four spin configurations are considered to determine the magnetic ground state of monolayer Fe_2C (see Figs. S1(a)–S1(d) in the Supplemental Material [59]). The DFT + U calculations with U_{LR} show that the AFM-1 state has the lowest energy (see Fig. S1(e) in the Supplemental Material [59]). The AFM-1 configuration is composed of two FM sublattices coupled antiferromagnetically, leading to a zero net magnetization. To study the influence of the Hubbard U parameter on the magnetic state, we have examined the variation of the energy difference between the FM and AFM-1 states with the Hubbard U value. As shown in Fig. 1(b), the magnetic order of monolayer Fe_2C is strongly affected by the Hubbard U parameter. For $U \leqslant 2$, monolayer Fe_2C has the FM ground state, which is consistent with the previous studies with small U values [71–73]. For $U \geqslant 3$, there is a transition from FM to AFM-1 coupling between two iron layers. In the remainder of this paper, we have used the self-consistent Hubbard U correction, $U_{LR} = 4.66$ eV, for the DFT + U calculations to obtain the electronic structure and the magnetic properties of the AFM-1 Fe_2C monolayer.

The T-phase atomic configuration of the AFM-1 Fe_2C monolayer after atomic relaxation is shown in Fig. 1(a). The optimized lattice constant, the Fe-C bond length, and the vertical distance between two Fe layers are 2.90 Å, 1.96 Å, and 2.05 Å, respectively. The electronic band structure of the AFM-1 Fe_2C monolayer by considering the spin-orbit coupling (SOC) is plotted in the reducible first Brillouin zone in Fig. 1(c). In the presence of SOC, the electronic states are represented by spinors with nonzero spin-up and spin-down components. The AFM-1 Fe_2C monolayer is a semimetal that the conduction band minimum crosses the Fermi level at K points on the boundaries of the Brillouin zone. The valence band maximum crosses the Fermi level between the K and Γ points. This is equivalent to the injection of a portion of one valence electron into the conduction band. In the presence of time-reversal symmetry and inversion symmetry, the electronic bands are doubly degenerate, known as Kramers pairs [74]. The Kramers degeneracy is lifted due to the breaking of time-reversal symmetry in the magnetic materials. As a result, there is an asymmetry between the electronic bands in the entire first Brillouin zone. For example, one can see the asymmetry of valence bands between the $\pm K$ and Γ points. Due to the AFM-1 order and the equivalent chemical environment of two Fe atoms, their atomic projected density of states (PDOS) is similar (see Fig. S3 in the Supplemental Material [59]). Around the Fermi level, the Fe-3d orbitals have a larger contribution than the Fe-4s, Fe-4p, and C-3p orbitals. As a result, the PDOS of atomic 3d orbitals is plotted for one of the iron atoms in Fig. 1(d). The crystal field splits Fe-3d orbitals into a nondegenerate d_{z^2} orbital and twofold degenerate d_{xz}/d_{yz} and $d_{xy}/d_{x^2-y^2}$ orbitals. The d_{z^2} is deep below the Fermi level for both spin-up and -down states. The main contribution of the spin-up state in the Fe-3d orbitals close to the Fermi level arises from the two degenerate 3d orbitals.

Our DFT + U calculations show that the magnetic anisotropy energy is continuously enhanced by the rotation of magnetic moments from the out-of-plane to the in-plane direction (see Fig. S4 in the Supplemental Material [59]). As a result, the ground state of monolayer Fe_2C is AFM-1 with easy axis along the z direction (the hexagonal c direction). The DFT + U results are then mapped into the anisotropic Heisenberg Hamiltonian [Eq. (1)]. The magnetic exchange between nearest-neighbor Fe atoms, $J = 25.3$ meV, and the magnetic anisotropy, $D = 0.2$ meV, are derived from $E_{FMz} - E_{AFM-1z} = 12J$ and $E_{AFM-1z} - E_{AFM-1x} = 2D$, where AFM-1z and FMz are the AFM-1 and FM spin configuration along z, and AFM-1x is the AFM-1 spin configuration along the x axis. The value of magnetic anisotropy is small but crucially important to stabilize the finite-temperature long-range antiferromagnetic order. In the previous works, it has been shown that the values of nearest-neighbor and next-nearest-neighbor exchange interactions have the same order of magnitude in the FM ground state [71,72]. Based on our DFT + U results, the next-nearest-neighbor magnetic exchange parameter is estimated to be -2.7 meV, which is one order of magnitude smaller than the value of the nearest-neighbor exchange, so it has been ignored in the following (see Sec. 4 in the Supplemental Material [59]).

The anisotropic Heisenberg Hamiltonian is used to investigate the finite-temperature thermodynamics of the AFM-1 Fe_2C monolayer in the absence/presence of an external magnetic field. Considering the translational symmetry of the two sublattices, one can perform the Fourier transform of the Green's function to reciprocal sublattices,

$$\left\langle \left\langle S_{\lambda l}^+; e^{a S_{\mu m}^z} S_{\mu m}^- \right\rangle \right\rangle = \frac{2}{N} \sum_{\mathbf{k}} G_{\lambda \mu}(\mathbf{k}) e^{i\mathbf{k}.(\mathbf{R}_{\lambda l} - \mathbf{R}_{\mu m})}, \quad (8)$$

$$J_{\lambda l, \mu m} = \frac{2}{N} \sum_{\mathbf{k}} J_{\lambda \mu}(\mathbf{k}) e^{i\mathbf{k}.(\mathbf{R}_{\lambda l} - \mathbf{R}_{\mu m})}, \quad (9)$$

where $\mathbf{k}$ is a reciprocal lattice vector in the first Brillouin zone associated with each sublattice, $\mathbf{R}_{\lambda l}$ is a direct lattice vector for site l in sublattice λ, and $\frac{N}{2}$ is the number of sublattice sites. In the nearest-neighbor approximation, the Fourier transform of the exchange interaction is $J_{\lambda \mu}(\mathbf{k}) = J \sum_{\Delta} e^{-i\mathbf{k}.\Delta}$.

Utilizing the Fourier transform of the Green's function and the magnetic exchange interaction, the equation of motion [Eq. (7)] in the absence of a magnetic field can be written as

$$\left(E + 2J_{\lambda \nu}(\mathbf{0})\langle S_{\nu n}^z \rangle - 2D\langle S_{\lambda l}^z \rangle \right) G_{\lambda \mu}(\mathbf{k})$$
$$= \frac{\Theta_\lambda(a)}{2\pi} \delta_{\lambda, \mu} + 2J_{\lambda \nu}(\mathbf{k})\langle S_{\lambda l}^z \rangle G_{\nu \mu}(\mathbf{k})(\lambda \neq \nu), \quad (10)$$

where $\Theta_\lambda(a) \equiv \langle [S_\lambda^+, e^{a S_\lambda^z} S_\lambda^-] \rangle$.

In a zero external magnetic field, the magnetizations of two sublattices have equal values but opposite directions, $\langle S_A^z \rangle = -\langle S_B^z \rangle$. The matrix elements of $G(\mathbf{k})$ in the two-sublattice
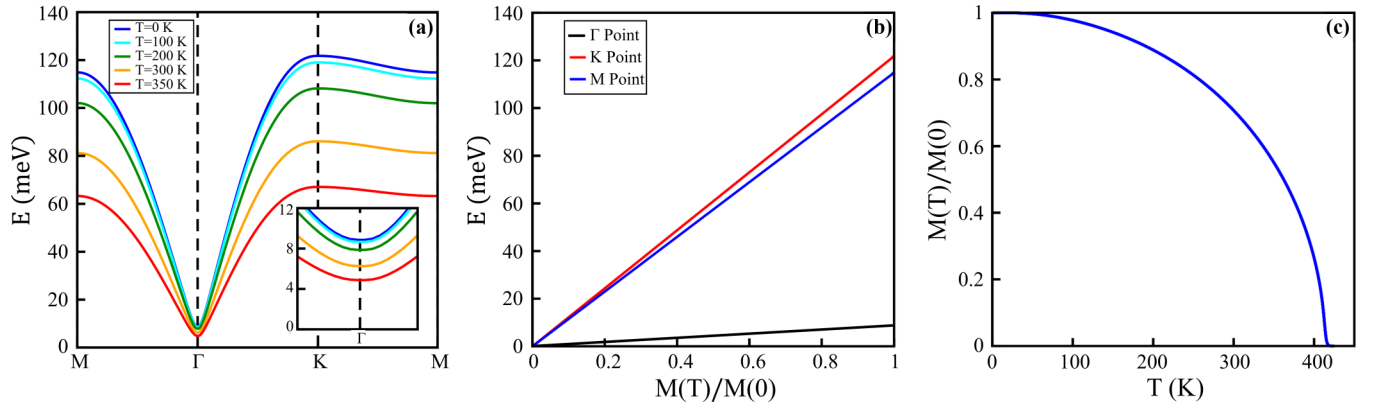
FIG. 2. (a) The magnon energy spectrum at different temperatures along a high-symmetry path in the first Brillouin zone. (b) The variation of temperature-dependent magnon energies with normalized magnetization at the Γ, K, and M high-symmetry points. (c) The temperature dependence of normalized sublattice magnetization for monolayer Fe$_2$C in the absence of an external magnetic field. The saturated sublattice magnetization $M(0)$ is 0.79 S.

model, A and B, are derived from Eq. (10) (see the Appendix),

$$G_{AA}(\mathbf{k}) = \frac{\Theta_A(a)}{2\pi} \left(\frac{E + (2J(0) + 2D)\langle S_A^z \rangle}{E^2 - \left(2J(0)\langle S_A^z \rangle + 2D\langle S_A^z \rangle\right)^2 - \left(2J(\mathbf{k})\langle S_A^z \rangle\right)^2} \right),$$

$$G_{BA}(\mathbf{k}) = -\frac{\Theta_A(a)}{2\pi} \left(\frac{2J(\mathbf{k})\langle S_A^z \rangle}{E^2 - (2J(0)\langle S_A^z \rangle + 2D\langle S_A^z \rangle)^2 - (2J(\mathbf{k})\langle S_A^z \rangle)^2} \right). \quad (11)$$

Due to the symmetry between two sublattices, G_{AA} and G_{BA} carry the same thermodynamic information as G_{BB} and G_{AB}. The poles of the Green's function determine the energy spec-

trum of two magnon branches inside the first Brillouin zone ($E_{u,d}$). In the absence of a magnetic field, the two magnon branches E_u and E_d in the Fe$_2$C unit cell are doubly degenerate,

$$E_{u,d} = E_0 = [2J(0) + 2D]\langle S_A^z \rangle \sqrt{1 - \left(\frac{2J(\mathbf{k})\langle S_A^z \rangle}{2J(0)\langle S_A^z \rangle + 2D\langle S_A^z \rangle} \right)^2}. \quad (12)$$

To investigate the thermodynamics of the AFM-1 monolayer, the correlation function is calculated within the spectral theorem [69],

$$\langle e^{aS_{\mu m}^z(t')} S_{\mu m}^-(t') S_{\lambda l}^+(t) \rangle = \lim_{\epsilon \to 0} i \int_{-\infty}^{+\infty} \left[\langle\langle S_{\lambda l}^+; e^{aS_{\mu m}^z} S_{\mu m}^- \rangle\rangle_{E+i\epsilon} - \langle\langle S_{\lambda l}^+; e^{aS_{\mu m}^z} S_{\mu m}^- \rangle\rangle_{E-i\epsilon} \right] \times \frac{e^{-iE(t-t')}}{e^{\frac{E}{k_B T}} - 1} dE. \quad (13)$$

In the limit of $t = t'$, the Fourier transform of the correlation function [Eq. (13)] is

$$\psi_{\lambda\mu}(\mathbf{k}, a) = \sum_{\mathbf{R}_{\lambda l} - \mathbf{R}_{\mu m}} \langle e^{aS_{\mu m}^z} S_{\mu m}^- S_{\lambda l}^+ \rangle e^{-i\mathbf{k}.(\mathbf{R}_{\lambda l} - \mathbf{R}_{\mu m})}. \quad (14)$$

The finite-temperature sublattice magnetization on each Fe atom can be derived from $\psi_{AA}(\mathbf{k}, a)$. By exploiting the Green's function [Eq. (11)], the correlation function is obtained via $\psi_{AA}(\mathbf{k}, a) = \Theta_A(a)\phi(\mathbf{k})$, where

$$\phi(\mathbf{k}) = \frac{1}{2E_0} \frac{E_0 + [2J(0)\langle S_A^z \rangle + 2D\langle S_A^z \rangle]}{e^{\frac{E_0}{k_B T}} - 1}$$
$$+ \frac{1}{2E_0} \frac{E_0 - [2J(0)\langle S_A^z \rangle + 2D\langle S_A^z \rangle]}{e^{-\frac{E_0}{k_B T}} - 1}. \quad (15)$$

Finally, the sublattice magnetization can be derived using algebraic procedures (see the Appendix for more details),

$$\langle S_A^z \rangle = \frac{(S_A - \Phi)(1 + \Phi)^{2S_A+1} + (S_A + \Phi + 1)\Phi^{2S_A+1}}{(1 + \Phi)^{2S_A+1} - \Phi^{2S_A+1}}, \quad (16)$$

where $\Phi \equiv \frac{1}{N} \sum_{\mathbf{k}} \phi(\mathbf{k})$. At the Néel temperature T_N, the sublattice magnetization tends to zero and, consequently, $\Phi \to \infty$. Therefore, one can expand Eq. (16) in the power of Φ^{-1} and estimate the Néel temperature,

$$\langle S_A^z \rangle = \frac{S_A(S_A + 1)}{3\Phi} + O(\Phi^{-2}). \quad (17)$$

Figure 2(a) shows the color plot of the magnon spectrum energy at different temperatures [Eq. (12)]. There is a magnon energy gap at the Γ point which guarantees the AFM-1 state at a finite temperature [9,10]. By increasing the temperature, the number of excited magnons increases which enhances the magnon-magnon interaction and renormalizes the energy spectrum [75]. As a result, the magnon energy gap is reduced with temperature, as shown in Fig. 2(a), and vanishes at temperatures above the Néel point. According to Fig. 2(b), the magnon energy spectrum is reduced by a factor of M/S, which is in agreement with the previous hypothesis of replacing S with thermal average $\langle S \rangle$ [15]. The sublattice magnetization dependence on temperature indicates the finite-temperature AFM-1 order, shown in Fig. 2(c). At low temperatures, the sublattice magnetization decreased slowly with temperature.
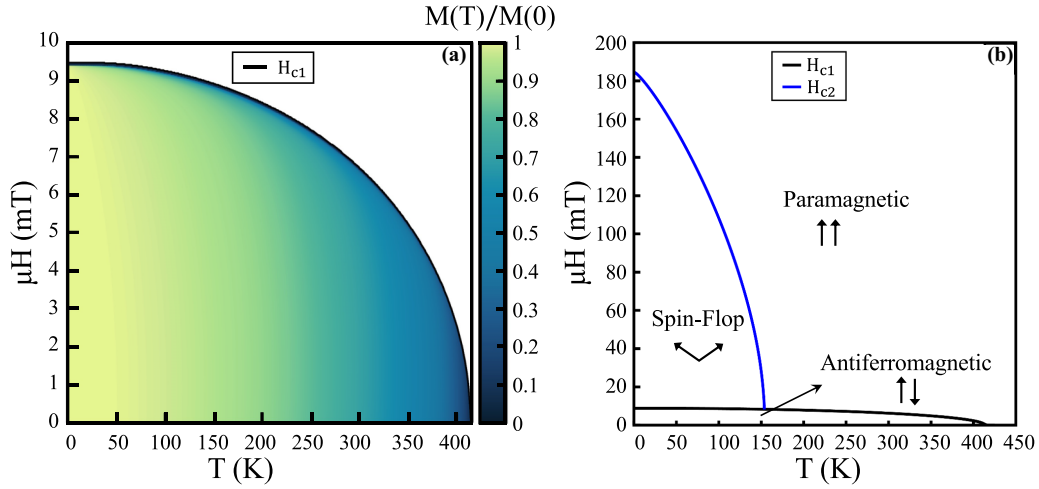
FIG. 3. (a) The variation of the normalized sublattice magnetization with temperature and external magnetic field for the AFM-1 ground state in monolayer Fe_2C. (b) The *H-T* phase diagram between AFM-1, paramagnetic, and spin-flop states in monolayer Fe_2C. The solid black and blue lines show the temperature-dependent critical magnetic fields for phase transitions from the AFM-1 to spin-flop and the spin-flop to paramagnetic phases, respectively.

At the higher-temperature regime, the magnon spectrum is softened (see Fig. 2(a) and see Fig. S5 in the Supplemental Material for a 3D presentation [59]) and the number of excited magnons increases sharply. The Néel point where the sublattice magnetization tends to zero is determined from Eq. (17) for monolayer Fe_2C at 390 K. To study the magnetic phase transition in the AFM-1 Fe_2C monolayer, an external magnetic field is applied along the easy-axis direction (perpendicular to the film). The AFM alignment of spins is sustained at the weak magnetic field and sufficiently low temperatures below the Néel point. In this case, the degeneracy of magnon energy is lifted into two branches,

$$E_u = E_H + \left(\mu H - \frac{1}{2}[2J(0) - 2D][\langle S_A^z \rangle + \langle S_B^z \rangle] \right),$$

$$E_d = E_H - \left(\mu H - \frac{1}{2}[2J(0) - 2D][\langle S_A^z \rangle + \langle S_B^z \rangle] \right), \quad (18)$$

where

$$E_H^2 = \frac{[2J(0) + 2D]^2(\langle S_A^z \rangle - \langle S_B^z \rangle) + 4J(\mathbf{k})^2(\langle S_A^z \rangle \langle S_B^z \rangle)}{4}. \quad (19)$$

Note that in the limit of $H \to 0$, the two magnon branches are degenerated, $E_u = E_d = E_0$. In the AFM-1 state, the sublattice magnetization of Fe_2C can be obtained by the Green's function approach [see Eq. (16)]. The Fourier transform of the correlation function [Eq. (13)] is

$$\psi(\mathbf{k}, a) = \frac{\Theta_A(a)}{4E_H} \frac{2E_H + [2J(0) + 2D](\langle S_A^z \rangle - \langle S_B^z \rangle)}{e^{\frac{E_u}{k_B T}} - 1}$$

$$- \frac{\Theta_A(a)}{4E_H} \{ 2E_H - [2J(0) + 2D](\langle S_A^z \rangle - \langle S_B^z \rangle) \}$$

$$\times \left(\frac{1}{e^{\frac{E_d}{k_B T}} - 1} + 1 \right). \quad (20)$$

The normalized sublattice magnetization at the different external magnetic fields is illustrated in Fig. 3(a). At low temperatures, the value of the sublattice magnetization is constant. By increasing the strength of the external magnetic field above the critical value H_{c1}, the alignment of sublattice magnetic moments changes from the *z* axis to the *x-y* plane,

$$\mu H_{c1} = E_0 + \frac{1}{2}[J(0) - 2D](\langle S_A^z \rangle + \langle S_B^z \rangle). \quad (21)$$

The solid black line in Fig. 3(a) indicates the critical magnetic field H_{c1}, which depends on temperature. In the presence of the external magnetic field, the magnon spectrum is split into two branches [see Eq. (18)]. For $H \geqslant H_{c1}$, the lower branch magnon becomes negative and the AFM-1 state is unstable. As a result, the AFM-1 to spin-flop phase transition occurs at a low-temperature regime. In the spin-flop phase, the AFM coupling of moments is maintained, while spins orient along the canted direction relative to the magnetic field, which results in the net magnetization along the easy axis.

The magnetic phase diagram for monolayer Fe_2C is illustrated in Fig. 3(b). The spin-flop is a metastable magnetic phase and, upon increasing H, the angle between spins and the magnetic field direction decreases to zero. As a result, there is a spin-flop to paramagnetic phase transition at H_{c2}. The value of the critical magnetic field H_{c2}, reduced by temperature, is

$$\mu H_{c2} = [2J(0) - 2D]\langle S_A^z \rangle. \quad (22)$$

At this critical point, the external magnetic field overcomes the exchange interaction between iron moments and the long-range intrinsic magnetic order disappears. The H_{c1} critical field competes with the magnetic anisotropy energy and brings moments into the hard plane (*x-y* plane). However, the value of H_{c2} is sufficiently large, which suppresses AFM coupling between iron atoms in the spin-flop phase. In monolayer Fe_2C, $J \gg D$ and, therefore, the value of H_{c2} is much greater than H_{c1}. For temperatures above 150 K, there is a direct AFM-1 to paramagnetic phase transition induced by an external magnetic field without the intermediate metastable spin-flop phase. The value of sublattice magnetization

decreases by thermal fluctuations until it drops to zero at the Néel point.

IV. CONCLUSIONS

In summary, we study the long-range intrinsic antiferromagnetic order using the combination of DFT + U and the Green's function formalism in monolayer Fe_2C. The DFT + U results are used to estimate the exchange interaction and the magnetic anisotropy in an effective Heisenberg spin model. The Heisenberg Hamiltonian with effective parameters is employed to investigate the thermodynamics of monolayer Fe_2C. Specifically, we calculate the doubly degenerated magnon spectrum and iron sublattice magnetization as a function of temperature in the random phase approximation. The magnon spectrum is linearly softened with temperature, which can be related to the lowering of sublattice magnetization. As a result, the sublattice magnetization vanishes at nearly 390 K for monolayer Fe_2C. We show the detailed magnetic phase diagram with antiferromagnetic, spin-flop, and paramagnetic phase regions. In the antiferromagnetic Fe_2C monolayer, there are two phase transitions induced by an applied external magnetic field along the easy axis. At low temperatures, there is a phase transition from the antiferromagnetic to spin-flop state. For $T > 150$ K, the antiferromagnetic phase is directly transformed into the paramagnetic spin configuration. The metastable spin-flop state is eventually converted into the paramagnetic phase at a critical magnetic field. The critical values of the external magnetic field as a function of temperature are calculated for both phase transitions (H_{c1} and H_{c2}). The presented formalism for monolayer Fe_2C is quite general and applicable for other 2D materials with the finite-temperature long-range antiferromagnetic order.

ACKNOWLEDGMENTS

APPENDIX: GREEN'S FUNCTION FORMALISM

Here we bring the details of the Green's function formalism and the random phase approximation for thermodynamic evaluation of a 2D spin system with antiferromagnetic coupling. The interaction between two magnetic moments localized at Fe sites is modeled in the form of an anisotropic Heisenberg Hamiltonian,

$$H = \sum_{i,j} J_{ij}\, \mathbf{S}_i.\mathbf{S}_j - \sum_i D\left(S_i^z\right)^2. \tag{A1}$$

Here, the summation is over the i and j sites which belong to the A and B sublattices, respectively,

$$\mathcal{H} = \sum_{i \in A}\sum_{j \in B} J_{i,j}\left[S_i^z S_j^z + \frac{1}{2}\left(S_i^+ S_j^- + S_i^- S_j^+\right)\right]$$
$$- D\left(\sum_{i \in A} S_i^z S_i^z + \sum_{j \in B} S_j^z S_j^z\right) - \mu H\left(\sum_{i \in A} S_i^z + \sum_{j \in B} S_j^z\right). \tag{A2}$$

The equation of motion for the Green's function is

$$E\langle\langle S_{\lambda l}^+, e^{aS_{\mu m}^z}S_{\mu m}^-\rangle\rangle = \frac{1}{2\pi}\langle[S_{\lambda l}^+, e^{aS_{\mu m}^z}S_{\mu m}^-]\rangle + \langle\langle[S_{\lambda l}^+, H], e^{aS_{\mu m}^z}S_{\mu m}^-\rangle\rangle. \tag{A3}$$

By definition, $G_{\lambda l,\mu m} = \langle\langle S_{\lambda l}^+, e^{aS_{\mu m}^z}S_{\mu m}^-\rangle\rangle$ and with the Fourier transform of Eq. (A3) with respect to time, one can obtain

$$EG_{\lambda l,\mu m} = \frac{\langle[S_{\lambda l}^+, e^{aS_{\mu m}^z}S_{\mu m}^-]\rangle}{2\pi}\delta_{\lambda l,\mu m} + \sum_{\nu,\kappa}\sum_{n,g}J_{\nu n,\kappa k}\left(\langle\langle[S_{\lambda l}^+, S_{\nu n}^z S_{\kappa k}^z], e^{aS_{\mu m}^z}S_{\mu m}^-\rangle\rangle + \frac{1}{2}\langle\langle[S_{\lambda l}^+, S_{\nu n}^+ S_{\kappa k}^-], e^{aS_{\mu m}^z}S_{\mu m}^-\rangle\rangle\right.$$
$$\left. + \frac{1}{2}\langle\langle[S_{\lambda l}^+, S_{\nu n}^- S_{\kappa k}^+], e^{aS_{\mu m}^z}S_{\mu m}^-\rangle\rangle\right) - \sum_\nu\sum_n D\langle\langle[S_{\lambda l}^+, S_{\nu n}^z S_{\nu n}^z], e^{aS_{\mu m}^z}S_{\mu m}^-\rangle\rangle. \tag{A4}$$

By using the random phase approximation [53], $\langle\langle S_{\nu n}^z S_{\lambda l}^+, S_{\mu m}^-\rangle\rangle = \langle S_{\nu n}^z\rangle\langle\langle S_{Al}^+, S_{\mu m}^-\rangle\rangle$, and the decoupling scheme used by Narath for the anisotropy term [70], $\langle\langle(S_{\lambda l}^+ S_{\lambda l}^z + S_{\lambda l}^z S_{\lambda l}^+); e^{aS_{\mu m}^z}S_{\mu m}^-\rangle\rangle \longrightarrow 2\langle S_{\lambda l}^z\rangle\langle\langle S_{\lambda l}^+; e^{aS_{\mu m}^z}S_{\mu m}^-\rangle\rangle$, Eq. (A4) becomes

$$EG_{\lambda l,\mu m} = \frac{\langle[S_{\lambda l}^+, e^{aS_{\mu m}^z}S_{\mu m}^-]\rangle}{2\pi}\delta_{\lambda l,\mu m} - 2\sum_{\substack{\nu \\ \nu \neq \lambda}}\sum_n J_{\nu n,\lambda l}\langle S_{\nu n}^z\rangle G_{\lambda l,\mu m} + 2\sum_{\substack{\nu \\ \nu \neq \lambda}}\sum_n J_{\nu n,\lambda l}\langle S_{\lambda l}^z\rangle G_{\nu n,\mu m} + 2D\langle S_{\lambda l}^z\rangle G_{\nu n,\mu m}. \tag{A5}$$

The Fourier transformations of G and J to the reciprocal lattice, given by Eqs. (8) and (9), are used on both sides of Eq. (A5),

$$EG_{\lambda\mu}(\mathbf{k}) = \frac{\Theta_\lambda(a)}{2\pi}\delta_{\lambda,\mu} - 2J_{\lambda\nu}(0)\langle S_\nu^z\rangle G_{\lambda\mu}(\mathbf{k}) + 2J_{\lambda\nu}(\mathbf{k})\langle S_\lambda^z\rangle G_{\nu\mu}(\mathbf{k}) + 2D\langle S_\lambda^z\rangle G_{\lambda\mu}(\mathbf{k}), \tag{A6}$$

where $\Theta_\lambda(a) \equiv \langle [S_{\lambda l}^+, e^{aS_{\lambda l}^z} S_{\lambda l}^-] \rangle$ and $J_{\lambda\mu}(\mathbf{k}) = J \sum_\Delta e^{-i\mathbf{k}.\Delta} \delta_{\lambda,\mu\pm1} = J(\mathbf{k})\delta_{\lambda,\mu\pm1}$ in the nearest-neighbor approximation. The AFM-1 monolayer contains two A and B sublattices. The Green's function elements are

$$G_{AA}(\mathbf{k}) = \frac{\Theta_A(a)}{2\pi} \left(\frac{E - \mu H + 2J(0)\langle S_A^z \rangle - 2D\langle S_B^z \rangle}{(E - E_u)(E + E_d)} \right), \tag{A7}$$

$$G_{BA}(\mathbf{k}) = \frac{\Theta_A(a)}{2\pi} \left(\frac{2J(\mathbf{k})\langle S_B^z \rangle}{(E - E_u)(E + E_d)} \right), \tag{A8}$$

$$G_{BB}(\mathbf{k}) = \frac{\Theta_B(a)}{2\pi} \left(\frac{E - \mu H + 2J(0)\langle S_B^z \rangle - 2D\langle S_A^z \rangle}{(E - E_u)(E + E_d)} \right), \tag{A9}$$

$$G_{AB}(\mathbf{k}) = \frac{\Theta_B(a)}{2\pi} \left(\frac{2J(\mathbf{k})\langle S_A^z \rangle}{(E - E_u)(E + E_d)} \right), \tag{A10}$$

where E_u and E_d are the magnon energies defined in Eq. (18). One can evaluate the spin correlation function [69], which is given by

$$\langle e^{aS_{Bm}^z} S_{Bm}^- S_{Al}^+ \rangle = \lim_{\epsilon \to 0} i \int_{-\infty}^{+\infty} \left[\langle\langle S_{Al}^+, e^{aS_{Bm}^z} S_{Bm}^- \rangle\rangle_{E+i\epsilon} - \langle\langle S_{Al}^+, e^{aS_{Bm}^z} S_{Bm}^- \rangle\rangle_{E-i\epsilon} \right] \frac{e^{-iE(t-t)}}{e^{\beta E} - 1} dE. \tag{A11}$$

yAfter Fourier transformation of both sides of Eq. (A11) and using definition $\psi(\mathbf{k}, a) \equiv \langle (e^{aS_B^z} S_B^-)(\mathbf{k}) S_A^+(\mathbf{k}) \rangle$, one can obtain the diagonal elements of the spin correlation function,

$$\psi(\mathbf{k}, a) = \frac{\Theta_A(a)}{4E_H} \left[\frac{2E_H + [2J(0) + 2D](\langle S_A^z \rangle - \langle S_B^z \rangle)}{e^{\frac{E_u}{k_B T}} - 1} - \{2E_H - [2J(0) + 2D](\langle S_A^z \rangle - \langle S_B^z \rangle)\} \left(\frac{1}{e^{\frac{E_d}{k_B T}} - 1} + 1 \right) \right]. \tag{A12}$$

E_H is defined in Eq. (19).

Next, we define

$$\phi(\mathbf{k}) \equiv \frac{1}{4E_H} \left[\frac{2E_H + [2J(0) + 2D](\langle S_A^z \rangle - \langle S_B^z \rangle)}{e^{\frac{E_u}{k_B T}} - 1} - \{2E_H - [2J(0) + 2D](\langle S_A^z \rangle - \langle S_B^z \rangle)\} \left(\frac{1}{e^{\frac{E_d}{k_B T}} - 1} + 1 \right) \right]. \tag{A13}$$

Here, $\Phi \equiv \frac{1}{N} \sum_{\mathbf{k}} \phi(\mathbf{k})$ and $\psi(a) \equiv \frac{1}{N} \sum_{\mathbf{k}} \psi(\mathbf{k}, a)$. As a result,

$$\psi(a) = \Phi \Theta_A(a). \tag{A14}$$

The commutation relation defining $\Theta_A(a)$ is simplified by the identity $[S_A^+, (S_A^z)^n] = \{(S_A^z - 1)^n - (S_A^z)^n\} S_A^+$. Hence,

$$\Theta_A(a) = 2\langle e^{aS_A^z} S_A^z \rangle + (e^{-a} - 1)\langle e^{aS_A^z} S_A^+ S_A^- \rangle. \tag{A15}$$

By the identity $S_A^z = S_A(S_A + 1) - (S_A^z)^2 - S_A^- S_A^+$, we substitute $S_A^+ S_A^-$ by terms of S_A^z,

$$\Theta_A(a) = S_A(S_A + 1)(e^{-a} - 1)\langle e^{aS_A^z} \rangle + (e^{-a} + 1)\langle e^{aS_A^z} S_A^z \rangle - (e^{-a} - 1)\langle e^{aS_A^z}(S_A^z)^2 \rangle. \tag{A16}$$

Next, we introduce the quantity $\Omega(a) \equiv \langle e^{aS_A^z} \rangle$ and the notation $\mathcal{D} \equiv \frac{d}{da}$,

$$\Theta_A(a) = S_A(S_A + 1)(e^{-a} - 1)\Omega(a) + (e^{-a} + 1)\mathcal{D}\Omega(a) - (e^{-a} - 1)\mathcal{D}^2\Omega(a) \tag{A17}$$

and

$$\psi(a) = \langle e^{aS_A^z} S_A^- S_A^+ \rangle = S_A(S_A + 1)\Omega(a) - \mathcal{D}\Omega(a) - \mathcal{D}^2\Omega(a). \tag{A18}$$

The differential equation of $\Omega(a)$ can be solved,

$$\Omega(a) = \frac{\Phi^{2S_A+1}e^{-S_A a} - (1 + \Phi)^{2S_A+1}e^{(S_A+1)a}}{[\Phi^{2S_A+1} - (1 + \Phi)^{2S_A+1}][(1 + \Phi)e^a - \Phi]}. \tag{A19}$$

Finally, the sublattice magnetization is

$$\mathcal{D}\Omega(a = 0) = \langle S_A^z \rangle = \frac{(S_A - \Phi)(1 + \Phi)^{2S_A+1} + (S_A + \Phi + 1)\Phi^{2S_A+1}}{(1 + \Phi)^{2S_A+1} - \Phi^{2S_A+1}}. \tag{A20}$$

In the absence of a magnetic field, $E_d = E_u = E_0$ which can be derived from Eq. (12).

[1] K. Khan, A. K. Tareen, M. Aslam, R. Wang, Y. Zhang, A. Mahmood, Z. Ouyang, H. Zhang, and Z. Guo, Recent developments in emerging two-dimensional materials and their applications, J. Mater. Chem. C **8**, 387 (2020).

[2] R. R. Nair, I.-L. Tsai, M. Sepioni, O. Lehtinen, J. Keinonen, A. V. Krasheninnikov, A. H. Castro Neto, M. I. Katsnelson, A. K. Geim, and I. V. Grigorieva, Dual origin of defect magnetism in graphene and its reversible switching by molecular doping, Nat. Commun. **4**, 2010 (2013).

[3] R. Nair, M. Sepioni, I.-L. Tsai, O. Lehtinen, J. Keinonen, A. Krasheninnikov, T. Thomson, A. Geim, and I. Grigorieva, Spin-half paramagnetism in graphene induced by point defects, Nat. Phys. **8**, 199 (2012).

[4] H. González-Herrero, J. M. Gómez-Rodríguez, P. Mallet, M. Moaied, J. J. Palacios, C. Salgado, M. M. Ugeda, J.-Y. Veuillen, F. Yndurain, and I. Brihuega, Atomic-scale control of graphene magnetism by using hydrogen atoms, Science **352**, 437 (2016).

[5] B. Li, T. Xing, M. Zhong, L. Huang, N. Lei, J. Zhang, J. Li, and Z. Wei, A two-dimensional Fe-doped SnS_2 magnetic semiconductor, Nat. Commun. **8**, 1958 (2017).

[6] D. Pal, S. Kumar, P. Shahi, S. Dan, A. Verma, V. K. Gangwar, M. Singh, S. Chakravarty, Y. Uwatoko, S. Saha *et al.*, Defect induced ferromagnetic ordering and room temperature negative magnetoresistance in MoTeP, Sci. Rep. **11**, 9104 (2021).

[7] C. Tang, Z. Zhang, S. Lai, Q. Tan, and W.-b. Gao, Magnetic proximity effect in graphene/$CrBr_3$ van der Waals heterostructures, Adv. Mater. **32**, 1908498 (2020).

[8] J. Ge, T. Luo, Z. Lin, J. Shi, Y. Liu, P. Wang, Y. Zhang, W. Duan, and J. Wang, Magnetic moments induced by atomic vacancies in transition metal dichalcogenide flakes, Adv. Mater. **33**, 2005465 (2021).

[9] N. D. Mermin and H. Wagner, Absence of Ferromagnetism or Antiferromagnetism in One- Or Two-Dimensional Isotropic Heisenberg Models, Phys. Rev. Lett. **17**, 1133 (1966).

[10] P. C. Hohenberg, Existence of long-range order in one and two dimensions, Phys. Rev. **158**, 383 (1967).

[11] P. Bruno, Spin-wave theory of two-dimensional ferromagnets in the presence of dipolar interactions and magnetocrystalline anisotropy, Phys. Rev. B **43**, 6015 (1991).

[12] V. Y. Irkhin, A. A. Katanin, and M. I. Katsnelson, Self-consistent spin-wave theory of layered Heisenberg magnets, Phys. Rev. B **60**, 1082 (1999).

[13] C. Gong, L. Li, Z. Li, H. Ji, A. Stern, Y. Xia, T. Cao, W. Bao, C. Wang, Y. Wang *et al.*, Discovery of intrinsic ferromagnetism in two-dimensional van der Waals crystals, Nature (London) **546**, 265 (2017).

[14] B. Huang, G. Clark, E. Navarro-Moratalla, D. R. Klein, R. Cheng, K. L. Seyler, D. Zhong, E. Schmidgall, M. A. McGuire, D. H. Cobden *et al.*, Layer-dependent ferromagnetism in a van der Waals crystal down to the monolayer limit, Nature (London) **546**, 270 (2017).

[15] J. L. Lado and J. Fernández-Rossier, On the origin of magnetic anisotropy in two dimensional CrI_3, 2D Mater. **4**, 035002 (2017).

[16] C. Xu, J. Feng, H. Xiang, and L. Bellaiche, Interplay between Kitaev interaction and single ion anisotropy in ferromagnetic CrI_3 and $CrGeTe_3$ monolayers, npj Comput. Mater. **4**, 57 (2018).

[17] I. Lee, F. G. Utermohlen, D. Weber, K. Hwang, C. Zhang, J. van Tol, J. E. Goldberger, N. Trivedi, and P. C. Hammel, Fundamental Spin Interactions Underlying the Magnetic Anisotropy in the Kitaev Ferromagnet CrI_3, Phys. Rev. Lett. **124**, 017201 (2020).

[18] T. Hattori, T. Miyamachi, T. Yokoyama, and F. Komori, Electronic and magnetic properties of the Fe_2N monolayer film tuned by substrate symmetry, J. Phys.: Condens. Matter **31**, 255001 (2019).

[19] M. Bonilla, S. Kolekar, Y. Ma, H. C. Diaz, V. Kalappattil, R. Das, T. Eggers, H. R. Gutierrez, M.-H. Phan, and M. Batzill, Strong room-temperature ferromagnetism in VSe_2 monolayers on van der Waals substrates, Nat. Nanotechnol. **13**, 289 (2018).

[20] D. J. O'Hara, T. Zhu, A. H. Trout, A. S. Ahmed, Y. K. Luo, C. H. Lee, M. R. Brenner, S. Rajan, J. A. Gupta, D. W. McComb *et al.*, Room temperature intrinsic ferromagnetism in epitaxial manganese selenide films in the monolayer limit, Nano Lett. **18**, 3125 (2018).

[21] J. Li, B. Zhao, P. Chen, R. Wu, B. Li, Q. Xia, G. Guo, J. Luo, K. Zang, Z. Zhang *et al.*, Synthesis of ultrathin metallic $MTe_2 (M = $ V, Nb, Ta) single-crystalline nanoplates, Adv. Mater. **30**, 1801043 (2018).

[22] Q. Li, M. Yang, C. Gong, R. V. Chopdekar, A. T. N'Diaye, J. Turner, G. Chen, A. Scholl, P. Shafer, E. Arenholz *et al.*, Patterning-induced ferromagnetism of Fe_3GeTe_2 van der Waals materials beyond room temperature, Nano Lett. **18**, 5974 (2018).

[23] Y. Deng, Y. Yu, Y. Song, J. Zhang, N. Z. Wang, Z. Sun, Y. Yi, Y. Z. Wu, S. Wu, J. Zhu *et al.*, Gate-tunable room-temperature ferromagnetism in two-dimensional Fe_3GeTe_2, Nature (London) **563**, 94 (2018).

[24] W. Yu, J. Li, T. S. Herng, Z. Wang, X. Zhao, X. Chi, W. Fu, I. Abdelwahab, J. Zhou, J. Dan *et al.*, Chemically exfoliated VSe_2 monolayers with room-temperature ferromagnetism, Adv. Mater. **31**, 1903779 (2019).

[25] W. Chen, Z. Sun, Z. Wang, L. Gu, X. Xu, S. Wu, and C. Gao, Direct observation of van der Waals stacking-dependent interlayer magnetism, Science **366**, 983 (2019).

[26] L. Kang, C. Ye, X. Zhao, X. Zhou, J. Hu, Q. Li, D. Liu, C. M. Das, J. Yang, D. Hu *et al.*, Phase-controllable growth of ultrathin 2D magnetic FeTe crystals, Nat. Commun. **11**, 3729 (2020).

[27] A. V. Kuklin, A. A. Kuzubov, E. A. Kovaleva, N. S. Mikhaleva, F. N. Tomilin, H. Lee, and P. V. Avramov, Two-dimensional hexagonal CrN with promising magnetic and optical properties: A theoretical prediction, Nanoscale **9**, 621 (2017).

[28] N. Luo, C. Si, and W. Duan, Structural and electronic phase transitions in ferromagnetic monolayer VS_2 induced by charge doping, Phys. Rev. B **95**, 205432 (2017).

[29] I. Miyazato, Y. Tanaka, and K. Takahashi, Accelerating the discovery of hidden two-dimensional magnets using machine learning and first principle calculations, J. Phys.: Condens. Matter **30**, 06LT01 (2018).

[30] W. Chen, Y. Kawazoe, X. Shi, and H. Pan, Two-dimensional pentagonal $CrX (X = $ S, Se, or Te) monolayers: Antiferromagnetic semiconductors for spintronics and photocatalysts, Phys. Chem. Chem. Phys. **20**, 18348 (2018).

[31] C. Zhang, Y. Nie, S. Sanvito, and A. Du, First-principles prediction of a room-temperature ferromagnetic JanusVSSe monolayer with piezoelectricity, ferroelasticity, and large valley polarization, Nano Lett. **19**, 1366 (2019).

[32] M. Modarresi, A. Mogulkoc, Y. Mogulkoc, and A. N. Rudenko, Lateral Spin Valve Based on the Two-Dimensional CrN/P/CrN Heterostructure, Phys. Rev. Appl. **11**, 064015 (2019).

[33] R. Han, Z. Jiang, and Y. Yan, Prediction of novel 2D intrinsic ferromagnetic materials with high Curie temperature and large perpendicular magnetic anisotropy, J. Phys. Chem. C **124**, 7956 (2020).

[34] K. Choudhary, K. F. Garrity, J. Jiang, R. Pachter, and F. Tavazza, Computational search for magnetic and nonmagnetic 2D topological materials using unified spin-orbit spillage screening, npj Comput. Mater. **6**, 49 (2020).

[35] B. G. Li, Y. F. Zheng, H. Cui, P. Wang, T. W. Zhou, D. D. Wang, H. Chen, and H. K. Yuan, First-principles investigation of a new 2D magnetic crystal: Ferromagnetic ordering and intrinsic half-metallicity, J. Chem. Phys. **152**, 244704 (2020).

[36] A. Mogulkoc, M. Modarresi, and A. N. Rudenko, Two-dimensional chromium pnictides $CrX(X = P, As, Sb)$: Half-metallic ferromagnets with high Curie temperature, Phys. Rev. B **102**, 024441 (2020).

[37] T. Marchandier, N. Dubouis, F. Fauth, M. Avdeev, A. Grimaud, J.-M. Tarascon, and G. Rousse, Crystallographic and magnetic structures of the VI_3 and $LiVI_3$ van der Waals compounds, Phys. Rev. B **104**, 014105 (2021).

[38] A. Mogulkoc, M. Modarresi, and A. N. Rudenko, Two-dimensional chromium bismuthate: A room-temperature Ising ferromagnet with tunable magneto-optical response, Phys. Rev. Appl. **15**, 064053 (2021).

[39] R. Basnet, A. Wegner, K. Pandey, S. Storment, and J. Hu, Highly sensitive spin-flop transition in antiferromagnetic van der Waals material MP_3 ($M =$ Ni and Mn), Phys. Rev. Mater. **5**, 064413 (2021).

[40] Y. Zhao, Y. Guo, S. Zhou, and J. Zhao, Xgt ($X =$ Fe, Mn, Cr; G = Ge; T = Te): A family of two-dimensional ternary intrinsic magnetic materials, Phys. Rev. Mater. **6**, 044005 (2022).

[41] M. B. Jungfleisch, W. Zhang, and A. Hoffmann, Perspectives of antiferromagnetic spintronics, Phys. Lett. A **382**, 865 (2018).

[42] M. Fiebig, N. P. Duong, T. Satoh, B. B. V. Aken, K. Miyano, Y. Tomioka, and Y. Tokura, Ultrafast magnetization dynamics of antiferromagnetic compounds, J. Phys. D: Appl. Phys. **41**, 164005 (2008).

[43] T. Jungwirth, J. Sinova, A. Manchon, X. Marti, J. Wunderlich, and C. Felser, The multiple directions of antiferromagnetic spintronics, Nat. Phys. **14**, 200 (2018).

[44] P. Wadley, B. Howells, J. Železný, C. Andrews, V. Hills, R. P. Campion, V. Novák, K. Olejník, F. Maccherozzi, S. Dhesi *et al.*, Electrical switching of an antiferromagnet, Science **351**, 587 (2016).

[45] K. Olejník, V. Schuler, X. Martí, V. Novák, Z. Kašpar, P. Wadley, R. P. Campion, K. W. Edmonds, B. L. Gallagher, J. Garcés *et al.*, Antiferromagnetic CuMnAs multi-level memory cell with microelectronic compatibility, Nat. Commun. **8**, 15434 (2017).

[46] K. Olejník, T. Seifert, Z. Kašpar, V. Novák, P. Wadley, R. P. Campion, M. Baumgartner, P. Gambardella, P. Němec, J. Wunderlich *et al.*, Terahertz electrical writing speed in an antiferromagnetic memory, Sci. Adv. **4**, eaar3566 (2018).

[47] J.-U. Lee, S. Lee, J. H. Ryoo, S. Kang, T. Y. Kim, P. Kim, C.-H. Park, J.-G. Park, and H. Cheong, Ising-type magnetic ordering in atomically thin $FePS_3$, Nano Lett. **16**, 7433 (2016).

[48] X. Wang, K. Du, Y. Y. F. Liu, P. Hu, J. Zhang, Q. Zhang, M. H. S. Owen, X. Lu, C. K. Gan, P. Sengupta *et al.*, Raman spectroscopy of atomically thin two-dimensional magnetic iron phosphorus trisulfide ($FePS_3$) crystals, 2D Mater. **3**, 031009 (2016).

[49] K. Kim, S. Y. Lim, J.-U. Lee, S. Lee, T. Y. Kim, K. Park, G. S. Jeon, C.-H. Park, J.-G. Park, and H. Cheong, Suppression of magnetic ordering in XXZ-type antiferromagnetic monolayer $NiPS_3$, Nat. Commun. **10**, 345 (2019).

[50] K. Kim, S. Y. Lim, J. Kim, J.-U. Lee, S. Lee, P. Kim, K. Park, S. Son, C.-H. Park, J.-G. Park *et al.*, Antiferromagnetic ordering in van der Waals 2D magnetic material $MnPS_3$ probed by raman spectroscopy, 2D Mater. **6**, 041001 (2019).

[51] S. Jiang, J. Shan, and K. F. Mak, Electric-field switching of two-dimensional van der Waals magnets, Nat. Mater. **17**, 406 (2018).

[52] D. R. Klein, D. MacNeill, Q. Song, D. T. Larson, S. Fang, M. Xu, R. A. Ribeiro, P. C. Canfield, E. Kaxiras, R. Comin *et al.*, Enhancement of interlayer exchange in an ultrathin two-dimensional magnet, Nat. Phys. **15**, 1255 (2019).

[53] S. V. Tiablikov, *Methods in the Quantum Theory of Magnetism*, 1st ed. (Springer, New York, 1967).

[54] N. Dalton and D. Wood, Critical behaviour of the simple anisotropic Heisenberg model, Proc. Phys. Soc. **90**, 459 (1967).

[55] J. Rusz, I. Turek, and M. Diviš, Random-phase approximation for critical temperatures of collinear magnets with multiple sublattices: GdX compounds ($X =$ Mg, Rh, Ni, Pd), Phys. Rev. B **71**, 174408 (2005).

[56] P. Giannozzi, S. Baroni, N. Bonini, M. Calandra, R. Car, C. Cavazzoni, D. Ceresoli, G. L. Chiarotti, M. Cococcioni, I. Dabo *et al.*, QUANTUM ESPRESSO: A modular and open-source software project for quantum simulations of materials, J. Phys.: Condens. Matter **21**, 395502 (2009).

[57] P. Giannozzi, O. Andreussi, T. Brumme, O. Bunau, M. B. Nardelli, M. Calandra, R. Car, C. Cavazzoni, D. Ceresoli, M. Cococcioni *et al.*, Advanced capabilities for materials modelling with QUANTUM ESPRESSO, J. Phys.: Condens. Matter **29**, 465901 (2017).

[58] H. J. Monkhorst and J. D. Pack, Special points for Brillouin-zone integrations, Phys. Rev. B **13**, 5188 (1976).

[59] See the Supplemental Material at http://link.aps.org/supplemental/10.1103/PhysRevB.106.174423 doi for (1) The spin configurations, (2) the convergence of the Hubbard U parameter, (3) the projected density of states for the Fe_2C monolayer, (4) the calculation of the next-nearest-neighbor magnetic exchange parameter, (5) the angular dependence of the magnetic anisotropy energy, and (6) the 3D presentation of the magnon energy spectrum. The Supplemental Material contains Refs. [35,76–78].

[60] R. Fletcher, *Practical Methods of Optimization* (Wiley, New York, 2013).

[61] E. German, R. Faccio, and A. W. Mombru, Comparison of standard DFT and Hubbard-DFT methods in structural and electronic properties of TiO_2 polymorphs and H-titanate ultrathin sheets for DSSC application, Appl. Surf. Sci. **428**, 118 (2018).

[62] H. Liu, A. Claisse, S. C. Middleburgh, and P. Olsson, Choosing the correct strong correlation correction for U_3Si_2: Influence of magnetism, J. Nucl. Mater. **527**, 151828 (2019).

[63] S. Memarzadeh, M. R. Roknabadi, M. Modarresi, A. Mogulkoc, and A. Rudenko, Role of charge doping and strain in the stabilization of in-plane ferromagnetism in monolayer VSe_2 at room temperature, 2D Mater. **8**, 035022 (2021).

[64] Y. Zhang, L.-F. Lin, A. Moreo, and E. Dagotto, Theoretical study of the crystal and electronic properties of α-RuI$_3$, Phys. Rev. B **105**, 085107 (2022).

[65] I. Timrov, N. Marzari, and M. Cococcioni, Hubbard parameters from density-functional perturbation theory, Phys. Rev. B **98**, 085127 (2018).

[66] C. Ricca, I. Timrov, M. Cococcioni, N. Marzari, and U. Aschauer, Self-consistent site-dependent $DFT+U$ study of stoichiometric and defective SrMnO$_3$, Phys. Rev. B **99**, 094102 (2019).

[67] I. Timrov, N. Marzari, and M. Cococcioni, Self-consistent Hubbard parameters from density-functional perturbation theory in the ultrasoft and projector-augmented wave formulations, Phys. Rev. B **103**, 045141 (2021).

[68] J. Crangle, *Solid State Magnetism* (Springer, New York, 1991).

[69] D. Zubarev, Double-time Green functions in statistical physics, Sov. Phys. Usp. **3**, 320 (1960).

[70] A. Narath, Zero-field ^{53}Cr nuclear magnetic resonance in ferromagnetic CrI$_3$: Renormalized spin-wave and Green's-function analysis, Phys. Rev. **140**, A854 (1965).

[71] Y. Yue, Fe$_2$C monolayer: An intrinsic ferromagnetic *MX*ene, J. Magn. Magn. Mater. **434**, 164 (2017).

[72] Y.-L. Li and P. Lv, First-principles study on the electric field manipulation of the magnetic property and the electronic structures for monolayer Fe$_2$C*MX*ene, Phys. Lett. A **386**, 126960 (2021).

[73] H. Hadipour and Y. Yekta, *Ab initio* study of the effective Coulomb interactions and stoner ferromagnetism in M_2C and M_2CO$_2$*MX*enes ($M =$ Sc, Ti, V, Cr, Fe, Zr, Nb, Mo, Hf, Ta), Phys. Rev. B **100**, 195118 (2019).

[74] D. Vanderbilt, *Berry Phases in Electronic Structure Theory: Electric Polarization, Orbital Magnetization and Topological Insulators* (Cambridge University Press, Cambridge, 2018).

[75] B. Wei, J.-J. Zhu, Y. Song, and K. Chang, Renormalization of gapped magnon excitation in monolayer MnBi$_2$Te$_4$ by magnon-magnon interaction, Phys. Rev. B **104**, 174436 (2021).

[76] I. Timrov, N. Marzari, and M. Cococcioni, HP - A code for the calculation of Hubbard parameters using density-functional perturbation theory, Comput. Phys. Commun. **279**, 108455 (2022).

[77] N. Majlis, *The Quantum Theory of Magnetism*, 2nd ed. (World Scientific, Singapore, 2007).

[78] Y.-L. Li and P. Lv, The tuning on the magnetism and the electronic structures of monolayer Ti$_2$N*MX*ene by electric field, Physica B: Condens. Matter **618**, 413183 (2021).